

Snow surface energy exchanges and snowmelt at a continental, midlatitude Alpine site

Donald W. Cline¹

Institute of Arctic and Alpine Research, University of Colorado, Boulder

Abstract. The objectives of this study were to measure and evaluate the energy balance of a continental, midlatitude alpine snowpack during spring snowmelt conditions, to relate variations in the energy budget and snowmelt to synoptic weather patterns, and to evaluate the performance of a point energy and mass balance model of a snow cover (SNTHERM) in alpine conditions. The investigation was conducted during the 1994 snowmelt season at Niwot Ridge (3517 m above sea level (asl); 40°03'N, 105°35'W) in the Colorado Front Range. Net radiative fluxes and net turbulent fluxes respectively provided 75% and 25% of the total energy available for snowmelt during the season. Sublimation losses were limited to only 4% of the initial snow water equivalence at the site. The largest energy available for snowmelt was associated with a ridge in the upper airflow over the central and southern Rocky Mountains that permitted warmer air into the region. Using measured data from the study site, the SNTHERM model estimated the disappearance of the snowpack just 3 days earlier than the observed 42-day ablation period.

1. Introduction

Understanding and predicting the response of hydrologic and biogeochemical transfers within snowmelt-dominated alpine basins to climate variability and change requires a thorough understanding of the energy transfers between the snowpack and the atmosphere that lead to changes in the internal energy of the snowpack and eventually cause snowmelt. The majority of snow energy exchange studies have been concerned with seasonal snowpacks at low elevations, in forested areas, on glaciers, or on sea ice [Kuusisto, 1986], and the substantial differences between conditions in these environments and conditions found in the alpine make comparisons complicated. Since relatively few studies have examined snowpack energy exchanges for entire snowmelt seasons or at high-altitude locations, our basic understanding of snowpack energy transfers in alpine areas is quite limited. Addressing this problem is the basic objective of this paper.

In general, radiative and turbulent transfer are the two most important processes affecting snow surface energy exchange. Additional, but frequently negligible, processes are energy exchanges between the base of the snowpack and the ground, and energy advected by rainwater [Obled and Harder, 1979; Male and Granger, 1981]. Most alpine snow energy balance studies have demonstrated that net radiation is the dominant source of energy for snowmelt, and that turbulent energy fluxes are typically small in magnitude and frequently of opposite sign so tending to cancel. *De la Casinière* [1974] provided an extreme case of this where the turbulent fluxes completely canceled over a 22-day period during snowmelt in the Vallee Blanche, in the French Alps, and 100% of the energy for snowmelt came

from net radiation. *Marks and Dozier* [1992] found that net radiation contributed 66–90% of the energy for snowmelt at two alpine sites near Emerald Lake in the Sierra Nevada of California. Similarly, *Calanaca and Heuberger* [1990] found that net radiation provided 88% of the energy for snowmelt in the arid climate of the Tianshan Mountains. Low magnitudes of the turbulent fluxes over alpine snow have been attributed to colder air temperatures typically found there [*Kirnbauer et al.*, 1994]. Strong winds often associated with alpine regions should increase the role of turbulent fluxes, but many alpine energy balance studies are performed in relatively sheltered valleys, whose lower wind speeds reduce turbulent flux magnitudes [*Plüss and Mazzoni*, 1994]. Exceptional cases where turbulent fluxes provided the dominant source of energy for snowmelt (57–82%) have been reported by *Prowse and Owens* [1982] and by *Moore and Owens* [1984] for two maritime alpine sites. Thus it is clear that the relative roles of radiative and turbulent energy exchanges in alpine snowmelt can vary considerably, and that net radiation is not always the dominant factor.

Large-scale air mass characteristics influence turbulent flux magnitudes at the point scale by affecting wind speed and atmospheric temperature and moisture. Similarly, net radiation magnitudes are influenced by air mass characteristics such as cloud type and amount. Thus seasonal climate variability should result in differences in the relative importance of radiative and turbulent fluxes to snowmelt during the course of the snowmelt season. *Male and Granger* [1981] recommended that relating energy exchanges at the point scale to larger-scale factors would provide more rapid practical understanding of the importance of snow energy balance components, but few studies have reported the relevant synoptic weather context. In one example, *Moore and Owens* [1984] showed that air mass and regional circulation indices explained 75% of the variance in the daily totals of turbulent fluxes during alpine snowmelt in New Zealand and concluded that since large-scale air mass characteristics are more predictable than local wind, temper-

¹Now at Office of Hydrology, National Weather Service, NOAA, Chanhassen, Minnesota.

ature, and relative humidity patterns, they were potentially more useful for predicting snowmelt. Although such an approach may be less useful in nonmaritime alpine areas where radiative fluxes typically dominate the snow energy balance, *Kuusisto* [1986] pointed out that very intense snowmelt usually requires a large turbulent transfer in addition to the radiative transfer. Thus synoptic weather patterns may be useful in continental alpine areas for determining or predicting periods of intense melt, but there have been no experiments conducted to evaluate relationships between continental midlatitude alpine snowpack energy exchanges and synoptic weather patterns.

Point snow energy balance experiments provide an opportunity to test physically based point snowmelt models under conditions characteristic of a specific location. Such models are increasingly used in a spatial context to meet the needs of a variety of hydrological, hydrochemical, and geomorphological applications in alpine regions [*Kirnbauer et al.*, 1994]. To build confidence in spatial applications of point snowmelt models in alpine basins, it is important to carefully evaluate model performance under alpine conditions.

This paper reports the results of an investigation of snow surface energy exchanges at a continental, midlatitude alpine site in Colorado over a complete snowmelt season. Radiative energy fluxes are measured directly, and turbulent energy exchanges are computed using an aerodynamic profile method. The overall role and importance of the individual components of the energy balance is described. Then differences in mean energy fluxes between different synoptic weather patterns are examined. Finally, energy balance results from a point energy and mass balance model of a snowcover (SNTHERM.89.rev4 [*Jordan*, 1991]) are compared to the experimental results. Comparison of SNTHERM-derived energy fluxes to those determined using the aerodynamic profile approach cannot validate either method [*Rastetter*, 1996], but if they are generally in agreement the comparison can be used to (1) corroborate the energy balance results and (2) provide confirmation that the coded representation of physical snowpack processes within SNTHERM is appropriate [*Oreskes et al.*, 1994].

2. Methods

2.1. Site Description

The data reported here were collected during the 1994 snowmelt season at Niwot Ridge on the eastern slope of the Front Range of Colorado (3517 m above sea level (asl); 40°03'N, 105°35'W). Niwot Ridge is a 10-km interfluvial extending eastward from the Continental Divide and is characterized by low rounded hills with shallow saddles in between. Tree line in this area is at approximately 3350 m. The instrument site is located in a relatively flat area within a broad saddle of the ridge.

The Front Range of Colorado has a dry continental climate due to its distance from the Pacific coast. Most of the precipitation received at Niwot Ridge arrives during early spring, as moist air from the Gulf of Mexico is drawn northward [*Barry*, 1992]. The high elevation and exposure of Niwot Ridge and typically dry atmospheric conditions result in large clear-sky atmospheric transmissivity, large insolation, low magnitudes of incident longwave radiation, low air temperatures, and high wind velocities. The depth of snow accumulation on Niwot Ridge is extremely variable, being influenced by the interaction of high wind velocities and topography. Windswept areas devoid of snow may be found immediately adjacent to deposi-

tional areas with accumulations in excess of 8 m. Records from a U.S. Department of Agriculture Natural Resources Conservation Service SNOTEL site located ≈5 km southeast of the study site indicate that the snowpack at the end of April 1994 was 97% of the average for the previous 12 years.

2.2. Energy Balance

Considered as a volume, the energy balance of a snowpack may be written as

$$\Delta Q_S + \Delta Q_M = Q^* + Q_H + Q_E + Q_G + Q_R \quad (1)$$

where ΔQ_S is the convergence or divergence of sensible heat fluxes within the snowpack volume, ΔQ_M is the latent heat storage change due to melting or freezing, Q^* is the net all-wave radiation flux, Q_H is the sensible heat flux, Q_E is the latent heat flux, Q_G is the ground heat flux, and Q_R is the heat advected by precipitation. Thus positive values of radiative and turbulent fluxes indicate a gain of energy in the snowpack, and negative values indicate a loss of energy in the snowpack. These changes in energy change either the temperature or the phase of the snowpack. This sign convention is used throughout the remainder of this paper. All data in this investigation were measured at 10-s intervals and averaged (or totaled where appropriate) every 10 min. Data were logged using a Campbell CR21x data logger and stored on a solid-state storage module.

Changes in the internal energy of the snowpack are calculated as a residual using (1). The residual term ($\Delta Q_S + \Delta Q_M$) was converted to mass units using the latent heat of fusion of water to allow comparison to measured snowmelt. The flow of heat through the soil was measured using a heat flux plate placed 0.05 m below the soil-snow interface. No significant heat exchange occurred through this level until the snowpack became very thin near the end of the snowmelt season. Therefore no further consideration of the ground heat flux will be given here. Also, as no rainfall events were observed during the study period, no further consideration will be given to the Q_R component of (1).

2.2.1. Radiative fluxes. The net all-wave radiation flux is the balance of the incident and reflected shortwave radiation and the incident and emitted longwave radiation and is expressed as

$$\begin{aligned} Q^* &= K \downarrow (1 - \alpha) + (L \downarrow - L \uparrow) \\ &= (K \downarrow - K \uparrow) + (L \downarrow - L \uparrow) \\ &= K^* + L^* \end{aligned} \quad (2)$$

where $K \downarrow$ is the incident shortwave radiation, α is the shortwave albedo of the snow surface, $K \uparrow$ is the reflected shortwave radiation, $L \downarrow$ is the incident longwave radiation, $L \uparrow$ is the emitted longwave radiation, K^* is the net shortwave radiative flux, and L^* is the net longwave radiative flux.

Incident and reflected shortwave radiative fluxes were measured using a Kipp and Zonen CM14 albedometer, which has two pyranometers (upward and downward looking) housed in a single instrument. Incident and upwelling longwave radiative fluxes were measured using a Kipp and Zonen CG2, again, a single housing containing upward and a downward looking pyrgeometers. Each pyrgeometer in the CG2 contains a thermistor adjacent to the sensor to permit temperature compensation of the longwave measurements. Net radiation fluxes reported in this paper were determined as shown by (2), using

Table 1. Instruments Used in This Study and Their Nominal Specifications

Parameter	Instrument	Model	Range	Accuracy
$K \downarrow, K \uparrow$	pyranometer	Kipp & Zonen CM14	305–2800 nm	$\pm 5\%$
$L \downarrow, L \uparrow$	pyrgeometer	Kipp & Zonen CG2	5–25 μm	$\pm 10\%$
T	thermistor	Vaisala HMP35C	-33° – 48°C	$\pm 0.4^{\circ}\text{C}$
RH	capacitance	Vaisala HMP35C	0–100%	$\pm 1\%$
u	propeller	Young 05103	0–60 m/s	$\pm 2\%$
P	capacitance	AIR-DB-2BX	475–825 mbar	± 0.01 mbar
Snowmelt	tipping bucket	CS-TE525	infinite	$\pm 1\%$ at ≤ 50 mm h^{-1}

the four individual components, but was also measured independently using a REBS Q*7 net radiometer to provide a check on the performance of the four radiometers. Characteristics of the shortwave and longwave radiometers are summarized in Table 1.

2.2.2. Turbulent fluxes. The sensible and latent heat fluxes were estimated using aerodynamic formulae with corrections for stability. The sensible heat flux through the surface boundary layer is expressed as

$$Q_H = \bar{\rho}(C_p) \left(\frac{k(\theta_2 - \theta_1)}{\phi_H[\ln(z_2/z_1)]} \right) \left(\frac{k(\mu_2 - \mu_1)}{\phi_M[\ln(z_2/z_1)]} \right) \quad (3)$$

and the latent heat flux is expressed as

$$Q_E = \bar{\rho}(L_v) \left(\frac{k(q_2 - q_1)}{\phi_E[\ln(z_2/z_1)]} \right) \left(\frac{k(u_2 - u_1)}{\phi_M[\ln(z_2/z_1)]} \right) \quad (4)$$

where $\bar{\rho}$ is the density of air, C_p is the specific heat of air at a constant pressure, L_v is the latent heat of vaporization of water, k is von Karman's constant, ϕ_H is the stability function for heat, ϕ_E is the stability function for water vapor, ϕ_M is the stability function for momentum, z_1 and z_2 are the instrument heights in the profile, θ_1 and θ_2 are the potential temperatures at the given profile height, q_1 and q_2 are the specific humidities at the given profile height, and u_1 and u_2 are the horizontal wind speeds at the given profile height.

The specific humidity at each level in the profile was determined by [Saucier, 1983]

$$q = \frac{0.622(e)}{P - 0.378(e)} \quad (5)$$

where P is the atmospheric pressure and e is the vapor pressure, calculated from the equation

$$e = \frac{e_s(RH)}{100} \quad (6)$$

where RH is the relative humidity at a given level, and e_s is the saturation vapor pressure over water, calculated from the equation

$$e_s = 6.11 \text{ mbar} \times 10^{aT/(T+b)} \quad (7)$$

Table 2. Equations Used for Calculations of Stability Functions in the Aerodynamic Profile Approach

Stability Function	Richardson Criteria		
	$Ri < -0.03$	$-0.03 \leq Ri \leq 0$	$0 < Ri < 0.19$
Φ_M	$(1 - 18Ri)^{-0.25}$	$(1 - 18Ri)^{-0.25}$	$(1 - 5.2Ri)^{-1}$
Φ_H, Φ_E	$1.3(\Phi_M)$	Φ_M	Φ_M

where T is the air temperature ($^{\circ}\text{C}$) at each level, a is a constant (7.5), and b is a constant (237.3°C). The stability functions were calculated as a function of the Richardson number (Ri) as described by Ohmura [1981] for use over Arctic snowcover using the equations shown in Table 2. The Richardson number was determined by

$$Ri = \frac{g}{\bar{\theta}} \left(\frac{\delta\theta/\delta z}{(\delta u/\delta z)^2} \right) \quad (8)$$

where g is the acceleration due to gravity and $\bar{\theta}$ is the mean potential temperature of the two levels.

Temperature and relative humidity were measured at three levels above the snow surface using Vaisala HMP35C temperature/relative humidity probes. Wind speed was also measured at three levels using R. M. Young 05103 anemometers. Characteristics of these instruments are summarized in Table 1. The instruments were mounted on a movable support attached to a fixed mast; the support was repositioned regularly to maintain instrument heights of 0.5, 1.0, and 2.0 m above the snow surface. Since relative magnitudes of these factors are of interest for the determination of gradients and not absolute magnitudes, the instruments were cross-calibrated with each other at the same level for 1 week before and after the snowmelt period to ensure that small differences could be measured in the profile. Using one instrument of each type as a standard, the other two were calibrated to fit the standard using linear regression equations. R^2 values for the regression fits were all greater than 0.99. The RMSE of the regression fits were less than 0.1°C for air temperature, about 0.5% for relative humidity, and less than 0.1 m s^{-1} for wind speed.

The estimation of turbulent fluxes as shown in (3) and (4) assumes that the fluxes are constant in the atmospheric layer being measured. However, during blowing snow conditions, sublimating ice particles act as sources of water vapor and losses of latent heat in the atmosphere, and the sensible and latent heat fluxes are not vertically constant [Morris, 1989]. In an effort to compensate for this problem, fluxes were calculated iteratively between 2.0 and 1.0 m, between 1.0 and 0.5 m, and between 2.0 and 0.5 m. The averages of these three flux-interval calculations are reported here. A more appropriate approach towards calculating the temperature and humidity profiles under blowing snow conditions is described by Schmidt [1982], but this approach was not feasible for this study.

2.3. Physical Snowpack Properties and Snowmelt

Two snow pits were excavated near the instrument tower at the beginning of the study period to measure physical properties of the snowpack. Vertical snow temperature profiles were measured at 0.1 m intervals using a digital thermometer. Snow density profiles were measured using a 1 L steel cutter following the protocol of Elder *et al.*, [1991].

Table 3. Initial Snowpack Conditions Used for SNTHERM

Node	Thickness, m	Temperature, K	Bulk Water Density, kg m^{-3}	Grain Size, mm	Material
18	0.002	273.1	348	0.5	snow
17	0.002	273.1	348	0.5	snow
16	0.1	273.1	348	0.5	snow
15	0.1	272.2	388	0.5	snow
14	0.1	271.7	476	0.5	snow
13	0.1	271.2	346	0.5	snow
12	0.1	270.7	354	0.5	snow
11	0.1	270.2	368	0.5	snow
10	0.1	270.7	402	0.5	snow
9	0.1	271.2	413	0.5	snow
8	0.1	271.7	371	0.5	snow
7	0.1	271.7	391	0.5	snow
6	0.1	272.2	378	1.0	snow
5	0.1	272.7	352	1.5	snow
4	0.1	272.7	336	1.5	snow
3	0.1	272.7	80	...	soil
2	0.3	273.5	100	...	soil
1	0.1	274.2	150	...	soil

These conditions were inferred from data from two snow pits excavated near the instrument tower, on April 19, 1994, and on April 29, 1994. The initial total snow depth was 1.3 m, the initial weighted mean bulk density was 379 kg m^{-3} , and the initial SWE was 0.49 m. The initial weighted mean snowpack temperature was 271.6 K, indicating a cold content of 5 mm liquid water.

Snowmelt was measured following the protocol of *Bales et al.* [1993] using two 1-m^2 draining lysimeters with 25-cm sidewalls. The lysimeters were located on the ground surface approximately 3 m from the instrument tower. The lysimeters were plumbed underground about 3 m into an underground shelter and instrument enclosure. Snowmelt from each lysimeter was measured inside the shelter using a Campbell Scientific TE525 tipping bucket gauge. The characteristics of this gauge are summarized in Table 1.

2.4. SNTHERM

SNTHERM is a comprehensive, physically based point energy and mass balance model of a snowcover that addresses surface temperature; transport of liquid water and water vapor; snow accumulation and ablation; densification; metamorphism; and their effect on the thermal and optical properties of the snowpack. The model is initialized with profiles of temperature, water content, and grain size for snowpack and soil strata, and the relevant governing equations are subject to meteorological boundary conditions [*Jordan, 1991*]. The methods used by SNTHERM to compute the surface energy budget are fundamentally different than the methods discussed above (hereafter referred to as "measured" fluxes, as opposed to the "modeled" SNTHERM fluxes). Whereas in the above method turbulent fluxes are computed using profile measurements of air temperature, relative humidity, and wind speed (with no surface measurements), SNTHERM computes turbulent fluxes using atmospheric measurements from only one height and model-derived snow surface temperature and relative humidity. SNTHERM employs corrections for atmospheric stability using slightly different functions than those shown in Table 2. The surface roughness length and bulk transfer coefficients are entered as user-defined parameters. Also, whereas in the measured approach all four components of the radiative balance are measured directly, SNTHERM computes the surface longwave emission based on model-derived snow surface

temperatures. Therefore in order for SNTHERM to correctly determine the snow surface characteristics used for the turbulent and radiative exchanges at each time step, it must first properly compute the internal snowpack energy and mass exchanges at the previous time step.

In this study the SNTHERM model was run using measured incident and reflected shortwave radiation; incident longwave radiation; and air temperature, relative humidity, and wind speed measurements from the 2.0-m level as inputs. The model is designed to accept measurements from a fixed reference height and ordinarily calculates the height of the instruments above the snow surface over time using its own calculation of changing snow depth. Since in this study the instruments were regularly raised or lowered to maintain specific instrument heights for the aerodynamic profile approach, the SNTHERM code was modified to accept this condition. SNTHERM was run for the same time period but on an hourly time step. The initial snowpack conditions used in the model are from the snow pit measurements and are shown in Table 3. A surface roughness length of 1 mm was used in the model, and bulk transfer coefficients were employed as recommended by *Jordan* [1991].

2.5. 500-mbar Synoptic Weather Patterns

Since the mean barometric pressure at the site during the study period was 650 mbar, the synoptic 500-mbar height conditions were considered most representative of the atmospheric conditions; the 750-mbar level generally intersects the terrain some 350 m lower in elevation from the site. The 500-mbar data are for 9:00 A.M. MST and were acquired from daily charts [*National Oceanic and Atmospheric Administration (NOAA), 1994*]. *Barry et al.* [1981] provided a catalogue of 31 synoptic scale climate patterns for the western United States using MSL pressure data in their analysis. No similar catalogue could be found for upper air patterns; for this study major air mass patterns were determined graphically by reviewing the daily direction of airflow and positions of isotherms on the charts. The resulting 500-mbar patterns resemble some of those identified by *Barry et al.* [1981], but these relationships are not pursued further here.

3. Results

The study period discussed in this paper began at maximum accumulation in the spring of 1994 (April 25, Julian Day (JD) 115) and continued through the full ablation of the snowpack (June 6, 1994, JD 157) until June 21 (JD 172). At the beginning of this study period the measured snow depth at the instrument site was 1.29 m, with 0.49 m water equivalence and a cold content of 5.0 mm.

3.1. Energy Fluxes

The albedo was approximately 0.90 on JD 115 following the last major accumulation of snow of the season (Figure 1a). The albedo then decreased over time, punctuated by brief increases on JD 123, 130, 145, and 148, when snowfall occurred. These snowfall events did not produce significant additional accumulation and either melted quickly or were blown off the older, harder snow surface such that the albedo quickly returned to pre-event levels. Following the disappearance of the snowpack, the tundra surface albedo remained near 0.2. The mean albedo for the entire snowmelt period was 0.66.

The influence of decreasing albedo on K^* is evident in

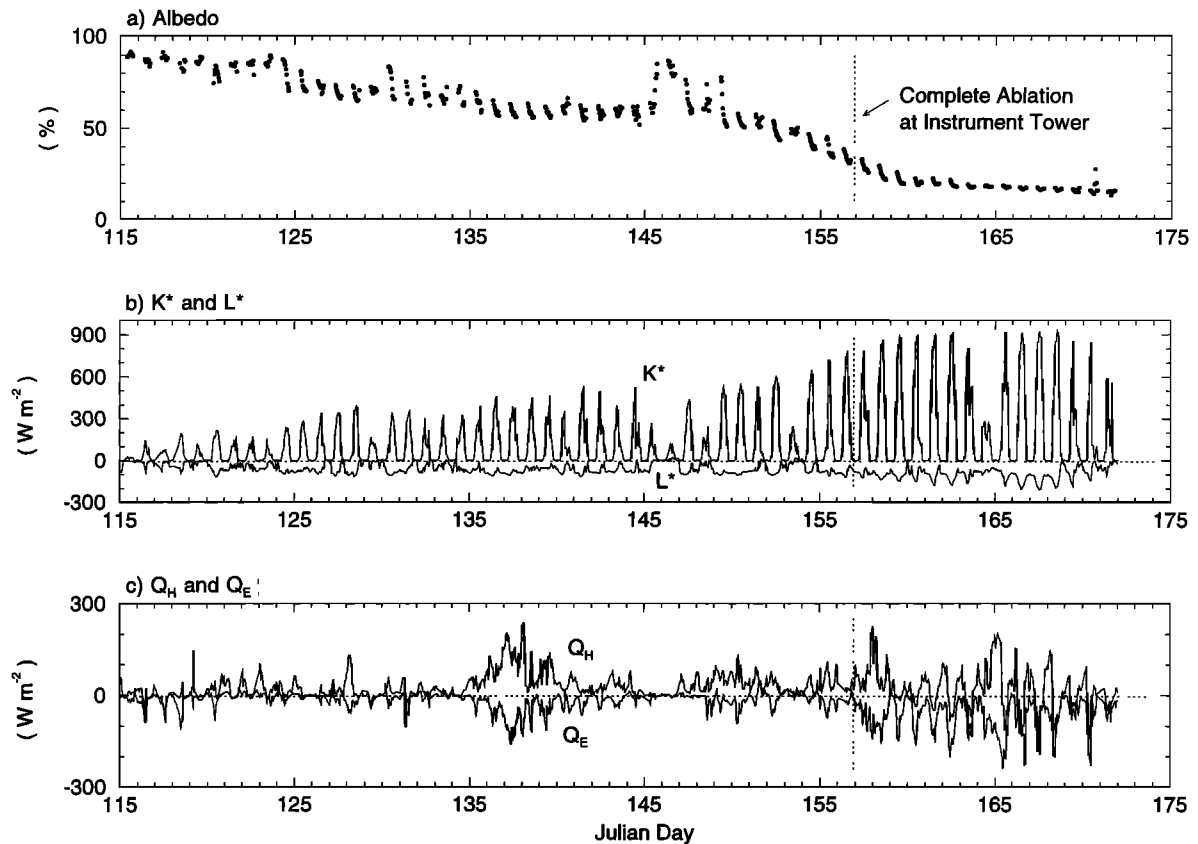


Figure 1. Seasonal patterns of snow surface albedo, and energy fluxes of K^* , L^* , Q_H , and Q_E . The points shown in the plot of albedo are only those that occurred while the cosine of the solar incidence angle was greater than 0.5 (solar elevation greater than 66°) to reduce errant values due to low sun angles.

Figure 1b. Although seasonal changes during the study period caused a gradual 7% increase in potential (exoatmospheric) peak incident solar radiation from 1218 to 1309 W m^{-2} (Figure 2), the changing albedo during the same time resulted in an order of magnitude larger increase in K^* from a daytime maximum of less than 100 W m^{-2} early in the season when the albedo was high, to nearly 800 W m^{-2} prior to complete disappearance of the snowpack.

Under clear atmospheric conditions, L^* losses of up to -126 W m^{-2} occurred (Figure 1b). Under overcast conditions $L \downarrow$ and $L \uparrow$ approximately balanced and L^* approached zero. Although the magnitude of L^* was much less than that of K^* , it was a relatively constant flux both day and night (unless clouds were present) compared to K^* , which of course was nonzero only during the daytime. The mean daily L^* was -58.3 W m^{-2} . Although the mean daytime K^* was 190.6 W m^{-2} , the mean daily K^* (both day and night) was only 96.5 W m^{-2} . Therefore over the entire snowmelt season, radiative processes resulted in a mean rate of energy flow directed towards the snowpack of only 38.2 W m^{-2} . Q_H was almost always a source of energy to the snow surface, with a mean value of 28.4 W m^{-2} (Figure 1c). Conversely, Q_E was almost always an energy loss with a mean of -15.6 W m^{-2} (Figure 1c). Similar to the net radiative exchanges, the turbulent transport processes resulted in a 12.8 W m^{-2} mean flow of energy directed towards the snowpack.

The fluxes of K^* , L^* , Q_H , and Q_E were integrated to determine the total amount of energy supplied by each. As indicated by the mean flux values, K^* and Q_H were energy

sources, contributing a season total of 349.6 and 103.0 MJ m^{-2} (77% and 23% of total energy gain) respectively; L^* and Q_E were energy losses, with total losses of -211.3 and -56.7 MJ m^{-2} (79% and 21% of total loss), respectively. The net energy gain over the period was 184.6 MJ m^{-2} . The cumulative totals over time for each component (Figure 3a) indicate that these relationships between the gains and losses remained fairly stable throughout the snowmelt season. Prior to JD 125, Q^* remained approximately balanced by net turbulent losses (Figure 3b). After JD 125 the net turbulent transfer was positive. This change in sign coincided with the onset of recorded melt draining from the base of the snowpack, discussed below. By the end of snowmelt, net radiative fluxes provided 75% of the total energy available for snowmelt, while the net energy supplied by turbulent sources was 25% of the seasonal total.

3.2. Energy Balance, Snowmelt, and Sublimation

The snowpack energy balance was calculated using (1). For snowmelt from a ripened snowpack to begin on a given day, the energy deficit from the previous night must first be satisfied. Therefore, to calculate snowmelt from the energy balance, a daily budget of hourly losses and gains was calculated for the residual energy term ($\Delta Q_S + \Delta Q_M$). The snowpack typically lost energy at night between about 6:00 P.M. and 6:00 A.M., and gained energy during the daytime hours (the specific times varied but were usually within an hour or two of 6:00 A.M. and 6:00 P.M.). Once daily snowmelt began, the nightly deficit was typically satisfied by between 10:00 A.M. and noon. The

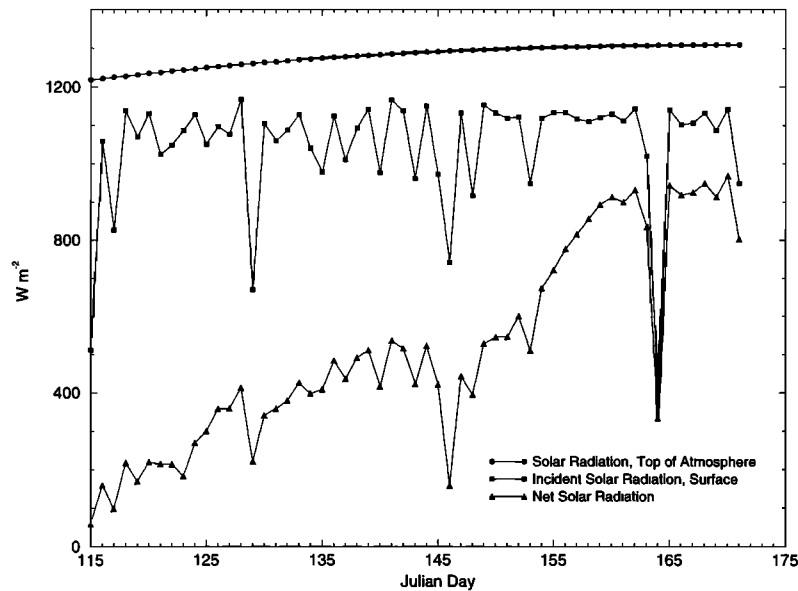


Figure 2. Comparison of daily maximum K^* to daily maximums of incident solar radiation at the surface (measured at the site) and solar radiation incident at the top of the atmosphere (calculated using algorithms prescribed by the *World Meteorological Organization* [1986]). The seasonal increase in K^* is an order of magnitude larger than the increase in potential radiation occurring at the same time, due to the gradually decreasing albedo of the snowpack. While not discussed in the text, it is interesting to note the apparent decrease in atmospheric transmissivity during the progression from spring to summer, as evidenced by the increasing difference between maximum insolation at the top of the atmosphere and at the surface. This would be consistent with other alpine observations as reported by Müller [1985].

progression of calculated melt through the season is shown in Figure 4, along with snowmelt measured at lysimeter 1.

Although calculated snowmelt began on JD 122, liquid water was not observed draining through the first lysimeter until JD 125. Since relatively large energy inputs to the snowpack may occur by late morning, once the previous night's energy deficit

was satisfied, the predicted snowmelt tended to increase rapidly from zero. For the first week of measured snowmelt (JD 125 to JD 131) the measured meltwater released at the base of the snowpack did not respond as suddenly; the hydrographs rose slowly over a 2- to 4-hour period and had shallow recession limbs. This period marks a transition between dry snow

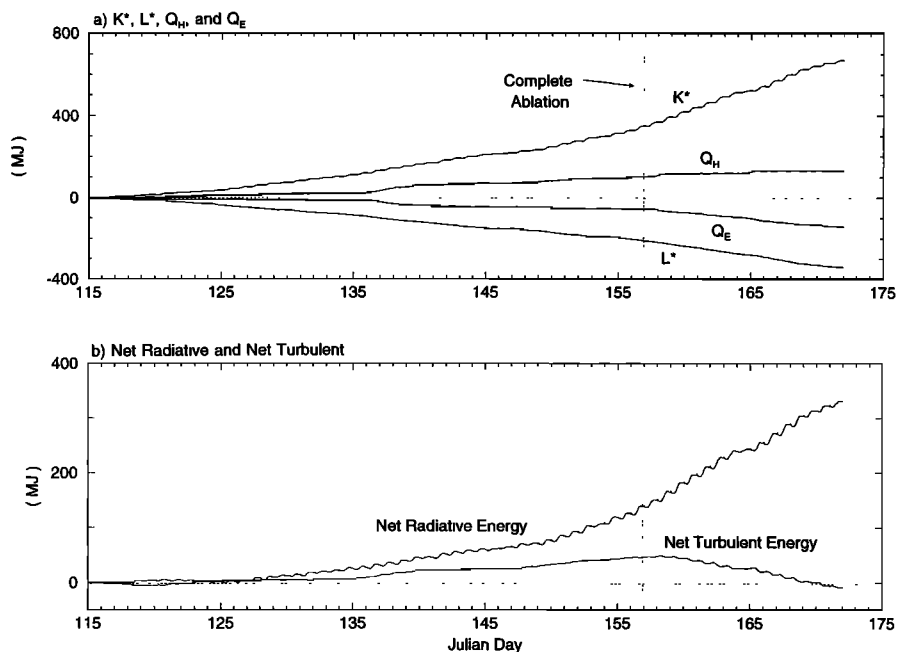


Figure 3. Cumulative totals of energy (MJ m^{-2}) over the snowmelt season: (a) individual fluxes of K^* , L^* , Q_H , and Q_E , and (b) net radiative fluxes and net turbulent fluxes.

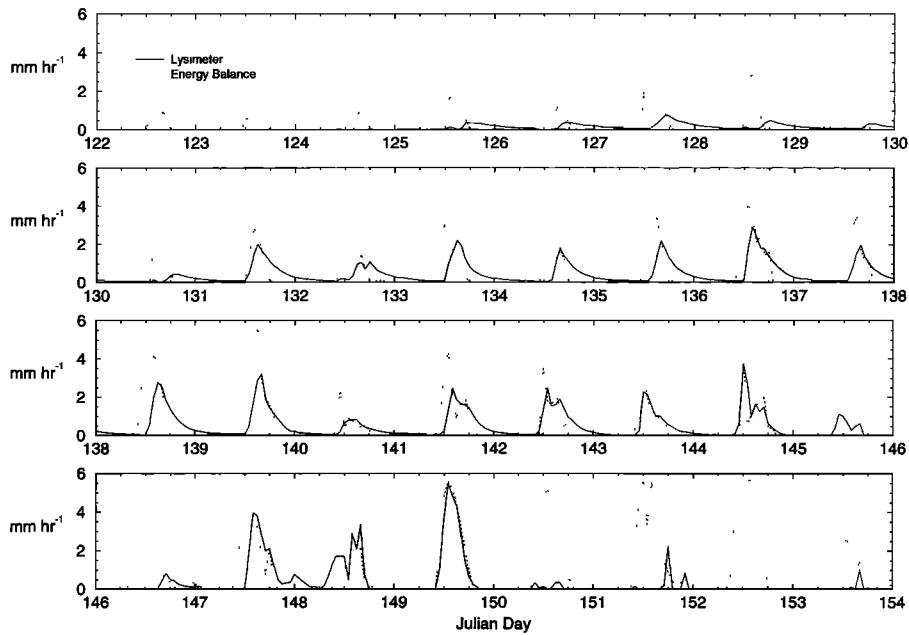


Figure 4. Daily patterns of snowmelt measured by a draining lysimeter and snowmelt calculated from the surface energy balance. Although by the energy balance snowmelt began on JD 122, it was not observed draining from the snowpack until JD 125. For the first 6 days of measured snowmelt, shallow rising limbs were indicative of capillary effects in the snowpack as the snowpack underwent a transition between cold and dry with small grains to a mature, ripe snowpack. Beginning JD 131, the measured hydrographs more closely resemble the calculated snowmelt.

with smaller grains and mature, ripe snow: a period during which capillary effects are clearly important but about which relatively little is known [Colbeck, 1978]. Following JD 131, the measured hydrograph had a steeper rising limb and more closely resembled theoretical flow expected for noncapillary, unsaturated gravity drainage [Colbeck, 1978].

The cumulative total of snowmelt calculated from ($\Delta Q_S +$

ΔQ_M) is shown in Figure 5a along with the cumulative total of snowmelt measured at lysimeter 1. Results from lysimeter 2 are not shown, as it measured flow rates an order of magnitude larger than those of lysimeter 1, and the total volume of water collected was similarly an order of magnitude larger than the volume of water that would have been in the snowpack column above the lysimeter, based on measured snow water equivalent

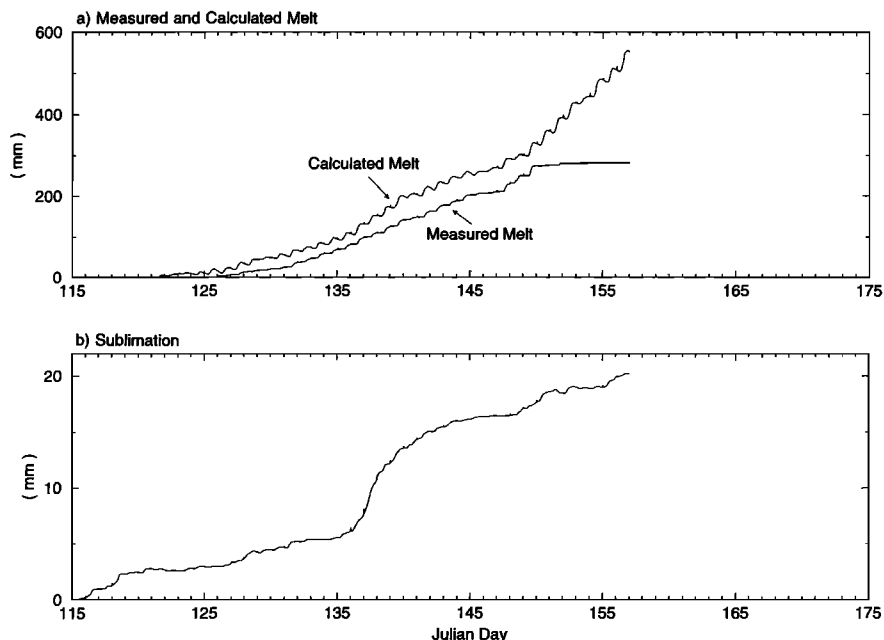


Figure 5. (a) Cumulative totals over the snowmelt season of (a) measured snowmelt, snowmelt calculated from the energy balance, and (b) sublimation calculated from the latent heat flux.

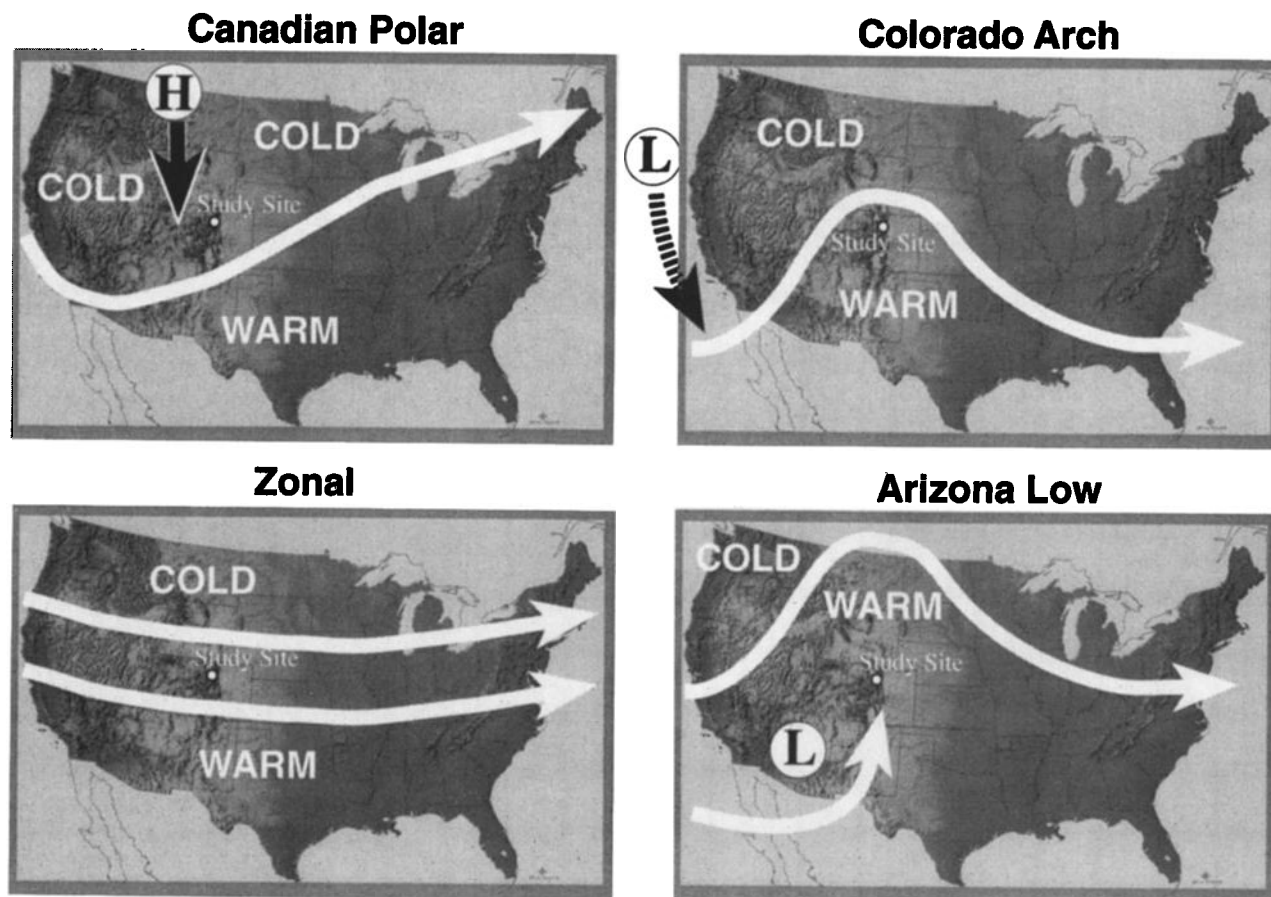


Figure 6. Four major 500-mbar synoptic weather patterns identified during the period of study: (a) Canadian Polar, (b) Zonal, (c) Colorado Arch, and (d) Arizona Low. The thick lines with arrowheads show the generalized airflow associated with the pattern and generally follow the isotherms for each pattern, which tend to indicate the meridional location of warm and cold air masses.

(SWE). These discrepancies indicate that the second lysimeter collected water preferentially from a much larger area than just above the lysimeter itself, preventing the use of those data here. Thus considering only the measured data from lysimeter 1 only, although the calculated melt began 3 days prior to the measured melt, it progressed at approximately the same rate as the measured melt. The total depth of calculated snowmelt was 555 mm. The difference in time between complete ablation at the instrument tower and the end of snowmelt at the lysimeter is explained simply by a slightly shallower snowpack at the lysimeter. Sublimation losses calculated from Q_E (shown in Figure 5b) amounted to an additional water loss of 20 mm.

By adding the calculated sublimation loss to the calculated snowmelt, the total calculated water content of the snowpack at the beginning of the season was 575 mm, a difference of 17% from the measured water equivalence at the beginning of the study period. Also, the relationship between surface snowmelt computed from the energy budget and meltwater efflux measured at the base of the snowpack behaved in an expected manner. These results suggest that the energy fluxes computed using this method were reasonably accurate.

3.3. Energy Flux Relationships With 500 mbar Synoptic Weather Patterns

Four major synoptic patterns were identified (Figure 6, Table 4) during the study period:

Pattern 1: Canadian Polar (6 days). This pattern is characterized by high pressure over western Canada that pushed cold and dry air southward into the Rocky Mountain region.

Pattern 2: Zonal (8 days). Under zonal conditions, air flowed directly west to east from off the coast of California, passing over Colorado. Isotherms during these conditions were nearly parallel and extended west-east, with no major longitudinal flow occurring.

Table 4. Chronological Sequence of Synoptic 500-mbar Weather Patterns During the Study Period

Julian Day	Pattern
115–120	CP
121–123	Z
124–128	CA
129–133	AL
134	Z
135–144	CA
145–146	AL
147–148	CA
149	Z
150–151	CA
152–156	Z

CP is the Canadian polar pattern, Z is the Zonal pattern, CA is the Colorado Arch pattern, and AL is the Arizona Low pattern.

Pattern 3: Colorado Arch (21 days). Low-pressure systems originating in the north Pacific moved southeastward down the coast of California. Upon making landfall, the centers of the lows tended to persist for a day or two over southern California. Even as the low-pressure centers approached from the north Pacific, the counterclockwise airflow around the low pulled warm air northward from off the coast of Baja. Downwind the airflow turned southward again, resulting in a large arch of warm air over much of the southwest and south central United States, with the apex of the arch centered over Colorado and Wyoming.

Pattern 4: Arizona Low (7 days). As discussed above, the low-pressure centers causing the Colorado Arch tended to persist over southern California for a day or two. Afterward, they tended to move over central or southeast Arizona. When this occurred, the large-amplitude airflow of the Colorado Arch persisted but was displaced northward with warm air flowing into the northern Rockies and into Canada. In Colorado, the airflow was then dominated by the counterclockwise flow of the low over Arizona until it dissipated, generally within a few days. While it remained over Arizona, the low continued to pull warm and moist air from west of Baja, but the airflow wrapped around the southern Rockies and the flow into north-central Colorado was from the south and southeast.

Mean air temperatures and specific humidities at the 2.0-m level were significantly different (99% confidence level) between each of the four patterns (Table 5) based on analysis of variance (ANOVA) tests. In an effort to compensate for potential serial correlation in hourly measurements, in these and subsequent ANOVAs the F tests were evaluated conservatively by reducing the degrees of freedom in the denominator to 120 for determining the critical value of F . The Canadian Polar pattern was the coolest, the only pattern with a mean air temperature below 0°C (-7.7°C), and was very dry, with a specific humidity of only 2.6 g m^{-3} . The warmest pattern was the Colorado Arch, with a mean air temperature of 4.6°C . The greatest atmospheric humidity occurred during the Arizona Low pattern with a mean specific humidity of 5.0 g m^{-3} .

Mean energy fluxes during each of these synoptic weather patterns were significantly ($P < 0.01$) different (Figure 7) based on ANOVA tests (Table 6). The Colorado Arch and Zonal patterns both resulted in net turbulent and net radiative energy gains, and subsequently there was more energy available to melt snow during these periods. The Canadian Polar and Arizona Low patterns both resulted in a net loss of turbulent energy with sensible heat gains but larger latent heat losses; net radiation was also negative during the Canadian Polar pattern so the snowpack lost energy during this period. Net radiation was positive and larger than the net turbulent loss during the Arizona Low period, so energy was available for snowmelt but at less than half the rate that occurred during the Colorado Arch and Zonal patterns.

Although the Zonal and Colorado Arch patterns both resulted in larger amounts of energy available for snowmelt, the Colorado Arch pattern was associated with nearly four times the mass loss due to sublimation than that which occurred with the Zonal pattern. There was no statistically significant difference in the 2.0- to 0.5-m-level wind speed gradients between these two synoptic patterns, but there was a large difference in the mean specific humidity gradients ($-0.0008\text{ g m}^{-3}\text{ m}^{-1}$ during the Zonal pattern, compared to $-0.0855\text{ g m}^{-3}\text{ m}^{-1}$ during the Colorado Arch pattern). Conditions were more stable during the Colorado Arch pattern than during the Zonal

Table 5. ANOVA Results Testing Whether Mean Air Temperatures and Specific Humidities Are Significantly Different During Different Synoptic Weather Patterns

Air Temperature, $^{\circ}\text{C}$				
Pattern	Mean	Standard Deviation	Standard Error	N
Canadian Polar	-7.7	2.9	0.3	123
Zonal	0.8	4.6	0.4	169
Colorado Arch	4.6	3.4	0.2	456
Arizona Low	1.7	2.5	0.2	168
Analysis of Variance				
Source of Variation	Sum of Squares	Degrees of Freedom	Mean Squares	F Test
Between patterns	14,699.7	3	4899.9	410.4
Within patterns	10,888.3	912	11.9	...
Total	25,588.0	915	28.0	...
Specific Humidity, g m^{-3}				
Pattern	Mean	Standard Deviation	Standard Error	N
Canadian Polar	2.6	0.5	0.1	123
Zonal	4.4	1.5	0.1	168
Colorado Arch	3.9	1.3	0.1	450
Arizona Low	5.0	1.0	0.1	155
Analysis of Variance				
Source of Variation	Sum of Squares	Degrees of Freedom	Mean Squares	F test
Between patterns	200,202.0	3	66,734.0	180.1
Within patterns	330,492.7	892	370.5	...
Total	530,694.8	895	593.0	...

Temperatures and humidities taken at 2-m level. All means are significantly different at greater than the 99% confidence level, even when potential serial correlation in the hourly data is compensated for by substantially reducing the degrees of freedom in the denominator (e.g., F_{critical} , d.f. = (3120), 1% significance level = 3.95).

(or any other) pattern, as indicated by a Richardson number significantly larger during the Colorado Arch pattern (0.03) than during the Zonal pattern (0.01); so while the magnitude of the calculated flux was dampened by a larger stability correction, the large difference in the latent heat fluxes between these two patterns was due mainly to differences in the humidity gradient.

3.4. SN THERM Results

While the observed snowpack ablation period lasted 42 days, full ablation of the snowpack occurred in 39 days in the SN THERM model run. Further comparison of SN THERM's modeled results to the previously described measured results are made below for Q_H , Q_E , $L \uparrow$, and $\Delta Q_S + \Delta Q_M$. These four energy budget terms depend on SN THERM's ability to represent internal snowpack processes, thus comparing these fluxes emphasizes the differences in the methods used in the two approaches.

The mean, standard deviation, and the overall RMSE between the observed fluxes and SN THERM fluxes are shown in Table 7. The RMSE, indicative in this case not of error per se but of differences between the two modeling approaches, was

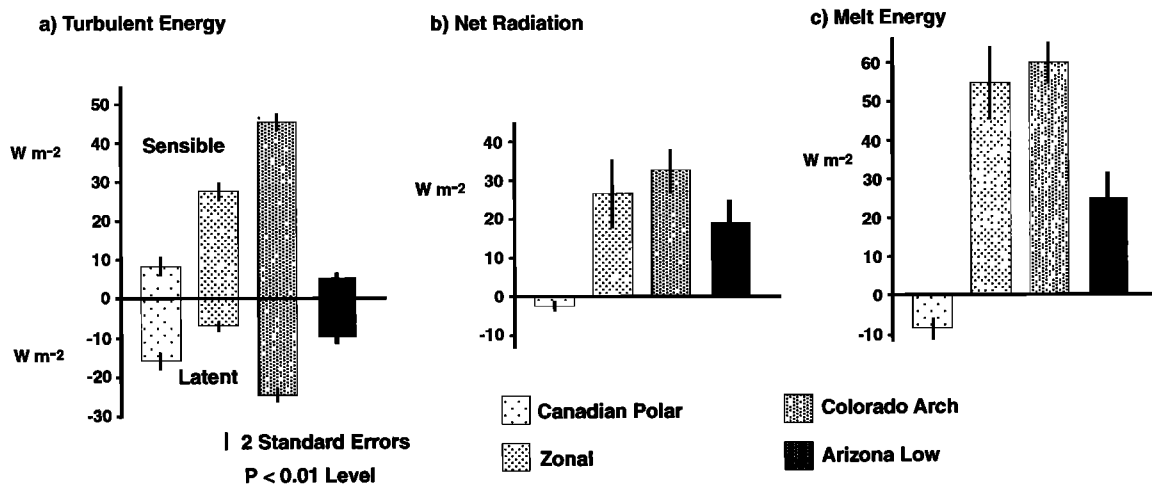


Figure 7. Bar plots showing the mean energy fluxes associated with each synoptic weather pattern: (a) turbulent fluxes of Q_H (all positive) and Q_E (all negative), (b) Q^* , and (c) $\Delta Q_S + \Delta Q_M$. An ANOVA test indicated that all the means are statistically different from one another at better than the 99% level; each bar includes a vertical line showing two standard errors.

of similar magnitude as the means for the two turbulent fluxes and for $\Delta Q_S + \Delta Q_M$. For $L \uparrow$ the RMSE was low (approximately 3%) with respect to the mean.

Scatterplots of modeled (SN THERM) fluxes with the mean hourly observed (atmospheric profile) fluxes (Figure 8) show that the two methods agreed well. SN THERM tended to compute larger magnitude turbulent fluxes (positive for Q_H and negative for Q_E) when fluxes were greater than 50–100 $W m^{-2}$. Most of the large fluxes (both positive and negative) occurred during the Colorado Arch synoptic pattern, when upper air temperatures were warmest, surface conditions were highly stable, and differences between methods used to determine and correct for stability in the two approaches were largest. The larger $\Delta Q_S + \Delta Q_M$ computed by SN THERM when $\Delta Q_S + \Delta Q_M$ exceeded $\approx 100 W m^{-2}$ coincided with the increased turbulent fluxes during the Colorado Arch pattern. SN THERM also tended to predict larger $L \uparrow$ than was measured when the measured $L \uparrow$ was lower than $\approx 290 W m^{-2}$; most of these observations occurred during the influence of the Canadian Polar synoptic pattern, when air and snow surface temperatures were well below freezing. These differences in longwave emissions could possibly indicate that SN THERM overpredicts snow surface temperatures during colder conditions, but given well-known difficulties associated with longwave radiation measurements, it is probably more likely that the differences are due to errors in the $L \uparrow$ measurements.

4. Discussion

The overall relative contributions of the separate energy balance components found in this study are compared to five other alpine snow energy budget studies in Table 8. The reported roles of net radiation and net turbulent energy exchanges for seasonal snowmelt varies between 100:0% to 18:82%. In the present study, net radiation only contributed three times the energy for melt over net turbulent transfer, in contrast to 5 to 10 times reported in the Sierra Nevada [Marks and Dozier, 1992] and the Tianshan [Calanca and Heuberger, 1990]. The results from Niwot Ridge are most similar to the ridge-top site in the Sierra Nevada and to the Tianshan study on glacier

1. In these three studies, net radiation provided from 66% to 88% of the energy for snowmelt, while net turbulent fluxes provided 12% to 32%.

Although it is common practice to report total contributions of the radiative and turbulent components of the energy balance, it is perhaps more useful to consider the variation in the roles of the different fluxes between the synoptic weather patterns that influence snow energy exchanges throughout the melt season (Figure 7), as has been done in some glacier studies [e.g., Brazel et al., 1992; Hay and Fitzharris, 1988]. There are at least two important points to be made concerning the differential responses of the overall energy balance and its individual components to different synoptic weather patterns that were observed here.

First, identifying such relationships suggests that there is potential for forecasting major changes in snow energy exchanges in mountain regions, insofar as we are able to forecast synoptic weather patterns. In particular, major response differences, such as the mean loss of energy from the snowpack during the Canadian Polar pattern contrasted with the large energy for snowmelt associated with the Colorado Arch pattern, at least provide a broad index that could be useful for forecasting the timing of snowmelt runoff from mountain regions.

Second, by relating actual snow energy budget response to observed climate variability, we establish a firmer foundation upon which to make predictions of alpine hydrologic response to climate change. For example, based on mean differences in temperature and humidity (Table 5), the four synoptic patterns observed in this study provide analogues for snowmelt response to cold/dry, warm/wet with enhanced precipitation, warm/wet without enhanced precipitation, and warm/dry climate scenarios. Since they are based on physical responses to actual climatic conditions, such analogues should be at least as useful as conceptual temperature index models for understanding and predicting how alpine hydrologic systems may respond to changes in climate characteristics.

The favorable comparison of SN THERM-derived energy fluxes to those determined using the aerodynamic profile

method does not, as mentioned previously, validate either method. However, since the two methods are based on fundamentally different approaches to determining the snowpack energy balance, greater confidence can be placed on the similar results. Furthermore, since SNTHERM must necessarily represent internal snowpack energy and mass exchanges properly in order to compute the energy balance, the corroborative evidence of the two approaches helps confirm that SNTHERM's representation of physical processes is correct. As noted previously, SNTHERM tended to predict larger magnitude turbulent fluxes than the aerodynamic method when fluxes were greater than $50\text{--}100\text{ W m}^{-2}$ (positive or negative);

Table 6. Results of ANOVA Tests to Determine Whether Mean Energy Fluxes Are Significantly Different During Different Synoptic Weather Patterns

Sensible Heat Flux				
Pattern	Mean	Standard Deviation	Standard Error	<i>N</i>
Canadian Polar	8.4	26.6	2.5	115
Zonal	27.7	27.7	2.3	155
Colorado Arch	44.4	44.9	2.2	427
Arizona Low	5.3	16.3	1.3	148
Analysis of Variance				
Source of Variation	Sum of Squares	Degrees of Freedom	Mean Squares	<i>F</i> Test
Between patterns	233,335.1	3	77,778.4	59.5
Within patterns	1,098,674.7	841	1306.4	...
Total	1,332,009.8	844	1578.2	...
Latent Heat Flux				
Pattern	Mean	Standard Deviation	Standard Error	<i>N</i>
Canadian Polar	-15.5	24.4	2.3	115
Zonal	-6.7	16.2	1.3	151
Colorado Arch	-24.9	32.8	1.6	416
Arizona Low	-9.6	18.4	1.7	115
Analysis of Variance				
Source of Variation	Sum of Squares	Degrees of Freedom	Mean Squares	<i>F</i> Test
Between patterns	47,600.9	3	15,867.0	21.3
Within patterns	590,856.7	793	745.1	...
Total	638,457.7	796	802.1	...
Net Radiation Flux				
Pattern	Mean	Standard Deviation	Standard Error	<i>N</i>
Canadian Polar	-2.4	31.2	2.8	124
Zonal	26.6	114.7	8.8	169
Colorado Arch	32.3	116.8	5.5	456
Arizona Low	18.8	76.8	5.9	168
Analysis of Variance				
Source of Variation	Sum of Squares	Degrees of Freedom	Mean Squares	<i>F</i> Test
Between patterns	123,647.1	3	41,215.7	3.95
Within patterns	9,521,711.8	913	10,429.0	...
Total	9,645,358.9	916	10,529.9	...

Table 6. (continued)

Residual Energy Term ($\Delta Q_S + \Delta Q_M$)				
Pattern	Mean	Standard Deviation	Standard Error	<i>N</i>
Canadian Polar	-8.4	28.3	2.6	115
Zonal	54.5	113.0	9.2	151
Colorado Arch	59.9	108.7	5.3	416
Arizona Low	35.0	74.0	6.9	115
Analysis of Variance				
Source of Variation	Sum of Squares	Degrees of Freedom	Mean Squares	<i>F</i> Test
Between patterns	445,445.4	3	148,481.8	15.63
Within patterns	7,532,842.2	793	9,499.2	...
Total	7,978,287.6	796	10,023.0	...

All flux values are in units of W m^{-2} . All means are significantly different area significant at greater than the 99% confidence level, even when potential serial correlation in hourly data is compensated for by substantially reducing the degrees of freedom in the denominator (e.g., F_{critical} , d.f. = (3,120), 1% significance level = 3.95).

most of these cases occurred during the Colorado Arch synoptic pattern when conditions were the most stable. Since the stability functions for stable conditions are nearly identical in the two methods ($\Phi_M = \Phi_H = \Phi_E = (1 - 5Ri)^{-1}$ in SNTHERM), the differences in large magnitude turbulent fluxes were most likely due to one of three factors: (1) differences in the bulk Richardson number used by SNTHERM and the profile Richardson number used in the aerodynamic method that are used to compute the stability correction, (2) the choice of user-defined roughness length used in this study, or (3) the choice of user-defined bulk transfer coefficients used here. No parameter fitting or model tuning was performed in this study; a mean roughness length for the season of 1 mm was computed during neutral conditions from the aerodynamic profile measurements, and Jordan's [1991] recommended bulk transfer coefficients were employed here. Further investigation will be necessary to determine the causes of the relatively minor methodological differences in the turbulent fluxes found in this study.

5. Conclusions

Snow surface energy exchanges were examined for a complete snowmelt season at a continental alpine site. Net radiative fluxes contributed 75% of the energy for snowmelt over the entire season, with turbulent fluxes contributing the re-

Table 7. Differences in Mean and Standard Deviations, and RMSE Between Fluxes Q_H , Q_E , $L \uparrow$, and $\Delta Q_S + \Delta Q_M$ Determined Using the Measured and Modeled Approaches

	Mean		Standard Deviation		RMSE
	Measured	SNTHERM	Measured	SNTHERM	
Q_H	29.6	44.8	39.7	51.3	33.1
Q_E	-17.9	-24.8	28.3	43.1	29.8
$L \uparrow$	302.3	301.0	18.7	15.2	8.9
$\Delta Q_S + \Delta Q_M$	45.5	50.5	100.1	122.6	53.7

All units are W m^{-2} .

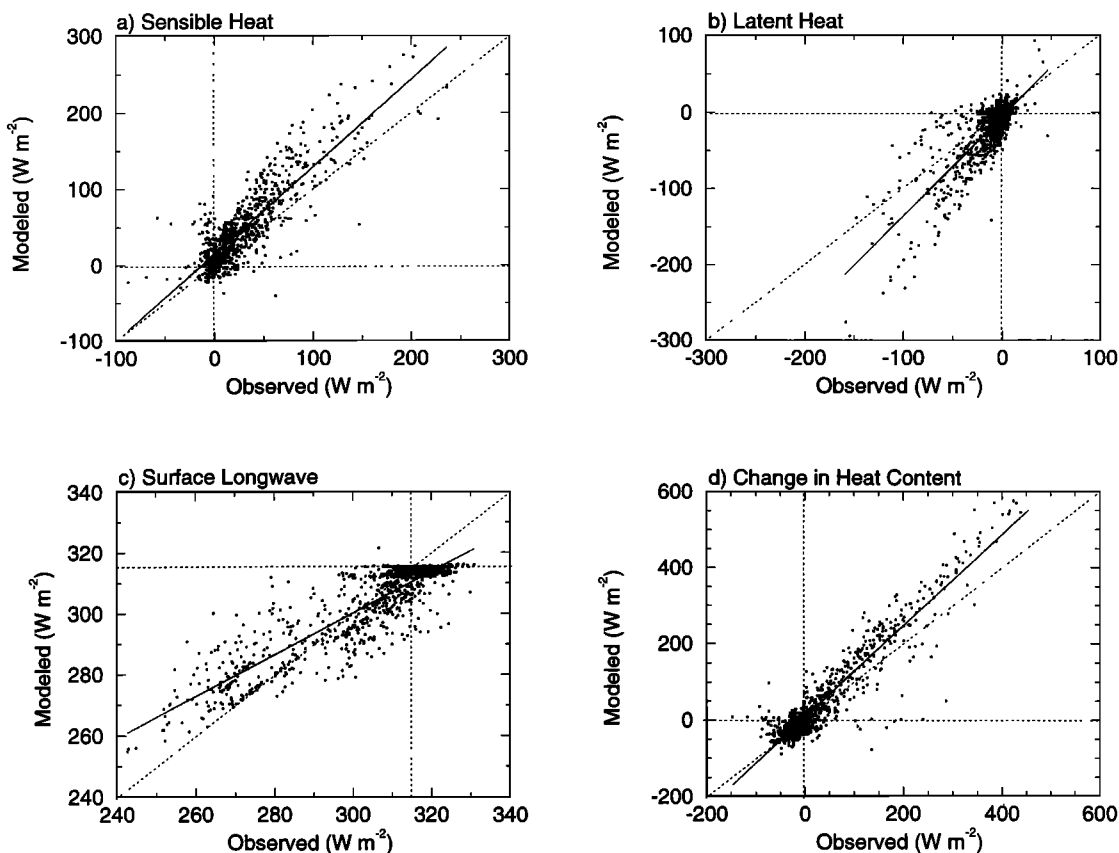


Figure 8. Scatterplots of mean hourly observed (measured radiative fluxes and atmospheric profile turbulent fluxes) and SNTHERM-modeled fluxes: (a) Q_H ; (b) Q_E ; (c) $L \uparrow$, with the dotted horizontal and vertical lines at 315 W m^{-2} , the longwave emission from a black body at 273.15 K ; and (d) $\Delta Q_S + \Delta Q_M$. The diagonal dotted lines are 1:1 correspondence lines, and the diagonal solid lines are regression fits.

maining 25%. These results are comparable with snow surface energy exchanges during snowmelt at other midlatitude alpine sites. Significant differences between individual energy fluxes and the overall energy balance were found between four different synoptic weather patterns; these differences may be useful for forecasting snow energy exchanges or as analogues for snowmelt response to climate variation and change. While the energy fluxes determined here were not rigorously validated (e.g., using eddy correlation methods), the fluxes were corroborated using a point energy and mass balance model for a snowpack (SNTHERM.89.rev4 [Jordan, 1991]) based on a fundamentally different approach to determining snowpack en-

ergy exchanges, with only minor differences found between flux magnitudes from the two approaches. The largest deviations in turbulent fluxes between the two approaches occurred during very stable atmospheric conditions associated with a single synoptic weather pattern. This comparison suggests that the representation of internal snowpack energy and mass exchange processes is generally correct, although further examination of SNTHERM parameters during very stable conditions is needed.

Snow energy exchange measurements will be continued at this site in the future as part of the Niwot Ridge Long-Term Ecological Research Program. Future work at the site will

Table 8. Comparative Snow Energy Balance Data for Selected Midlatitude Alpine Locations

Reference	Site	Elevation, m	Latitude, Longitude	Q^* , %	$Q_H + Q_E$, %	Record (days)	Dates
Present study	Niwot Ridge (Colorado)	3517	40N, 105W	75	25	42	April 25 to June 6, 1994
Calanca and Heuberger [1990]	Glacier 1 (Tianshan, China)	3910	44N, 87E	88	12	44	July 6 to Aug. 19, 1986
de la Casinière [1974]	Vallee Blanche (French Alps)	3550	46N, 7E	100	0	22	July 1–25, 1968
Marks and Dozier [1992]	Emerald Lake (Sierra Nevada)	3416	37N, 119W	82	16	31	May, 1986
				72	27	30	June, 1986
				66	32	31	July, 1986
Moore and Owens [1984]	Temple Basin (New Zealand)	1450	40S, 172W	16	82	12	Oct. 28 to Nov. 9, 1982
Prowse and Owens [1982]	Ski Basin	1500	43S, 172E	42	57	14	Nov. 15–28, 1976
				33	67	5	Oct. 26–30, 1977
				17	82	6	Oct. 24–29, 1979
				27	72	8	Oct. 22–29, 1980

include continued evaluation of relationships between point energy exchanges and synoptic weather patterns, further analysis of SNTHERM turbulent transfer parameters, and examination of meltwater flow pathways within the snowpack.

Please note that the micrometeorological data discussed in this paper are available electronically from the author.

Acknowledgments. This work could not have been completed without logistical and financial support provided by the Niwot Ridge Long-Term Ecological Research project (NSF DEB 9211776), the Mountain Research Station (BIR 9115097), the National Biological Service Global Change Research program (Colorado Rockies Biogeographic Area)(COLR-R92-0201), a Doctoral Dissertation Research Improvement grant from the NSF Geography and Regional Science program (SBR-9304604), and the NASA Earth Observing System program (NAGW-2602). Tim Bardsley and Mark Losleben provided field assistance for this project; Losleben also provided the atmospheric pressure data. Jim Robb provided the shaded-relief maps used in Figure 6. Mark Williams and Nel Caine provided valuable comments on the original draft of the manuscript. I am particularly grateful to David Tarboton and two anonymous reviewers who provided valuable comments that improved the manuscript.

References

- Bales, R. C., Davis, R. E., and M. W. Williams, Tracer release in melting snow: Diurnal and seasonal patterns, *Hydrol. Processes*, 7, 389–401, 1993.
- Barry, R. G., *Mountain Weather and Climate*, 2nd ed., Routledge, New York, 1992.
- Barry, R. G., G. Kiladis, and R. S. Bradley, Synoptic climatology of the western United States in relation to climatic fluctuations during the twentieth century, *J. Clim.*, 1, 97–113, 1981.
- Brazel, A. J., F. B. Chambers, and L. S. Kalkstein, Summer energy balance on the West Gulkana Glacier, Alaska, and linkages to a temporal synoptic index, *Z. Geomorphol. N. F. Suppl. Bd.*, 86, 15–34, 1992.
- Calanca, P., and R. Heuberger, Energy balance, in *Glacial Climate Research in the Tianshan, Zürcher Geogr. Schr.*, vol. 38, edited by A. Ohmura et al., pp. 60–70, *ETH Geogr. Inst.*, Zürich, 1990.
- Colbeck, S. C., The physical aspects of water flow through snow, in *Advances in Hydrosience*, vol. 11, Academic, San Diego, Calif., 1978.
- de la Casinière, A. C., Heat exchange over a melting snow surface, *J. Glaciol.*, 13(67), 55–72, 1974.
- Elder, K., J. Dozier, and J. Michaelson, Snow accumulation and distribution in an alpine watershed, *Water Resour. Res.*, 27(7), 1541–1552, 1991.
- Hay, J. E., and B. B. Fitzharris, The synoptic climatology of ablation on a New Zealand glacier, *J. Clim.*, 8, 201–215, 1988.
- Jordan, R., A one-dimensional temperature model for a snow cover, *Spec. Rep. 91-16*, U.S. Army Cold Reg. Res. and Eng. Lab., Hanover, N. H., 1991.
- Kirnbauer, R., G. Blöschl, and D. Gutknecht, Entering the era of distributed snow models, *Nord. Hydrol.*, 25(1/2), 1–24, 1994.
- Kuusisto, E., The energy balance of a melting snow cover in different environments, in *Modelling snowmelt-induced processes, IAHS Publ. 155*, pp. 37–45, 1986.
- Male, D. H., and R. J. Granger, Snow surface energy exchange, *Water Resour. Res.*, 17(3), 609–627, 1981.
- Marks, D., and J. Dozier, Climate and energy exchange at the snow surface in the alpine region of the Sierra Nevada, 2, Snow cover energy balance, *Water Resour. Res.*, 28(11), 3043–3054, 1992.
- Moore, R. D., and I. F. Owens, Controls on advective snowmelt in a maritime alpine basin, *J. Clim. Appl. Meteorol.*, 23, 135–142, 1984.
- Morris, E. M., Turbulent transfer over snow and ice, *J. Hydrol.*, 105, 205–223, 1989.
- Müller, H., Review paper on the radiation budget in the Alps, *J. Clim.*, 5, 445–462, 1985.
- National Oceanic and Atmospheric Administration, (NOAA), Daily weather maps, Silver Spring, Md., 1994.
- Obed, C., and H. Harder, A review of snow melt in the mountain environment, in *Proceedings on Modeling of Snowcover Runoff*, edited by S. C. Colbeck and M. Ray, pp. 179–204, U.S. Army Cold Regions Res. Eng. Lab., Hanover, N. H., 1979.
- Ohmura, A., Climate and energy balance on arctic tundra, Axel Heiberg Island, Canadian Arctic Archipelago, Spring and Summer 1969, 1970, and 1972, in *Zürcher Geographische Schriften*, vol. 3, 447 pp., *ETH Geogr. Inst.*, Zürich, 1981.
- Oreskes, N., K. Shrader-Frechette, and K. Belitz, Verification, validation, and confirmation of numerical models in the earth sciences, *Science*, 263, 641–646, 1994.
- Plüss, C., and R. Mazzoni, The role of turbulent heat fluxes in the energy balance of high alpine snowcover, *Nord. Hydrol.*, 25(1/2), 25–38, 1994.
- Prowse, T. D., and I. F. Owens, Energy balance over melting snow, Craigieburn Range, New Zealand, *J. Hydrol. N. Z.*, 21(2), 133–147, 1982.
- Rastetter, E. B., Validating models of ecosystem response to global change, *Bioscience*, 46(3), 190–198, 1996.
- Saucier, W. J., *Principles of Meteorological Analysis*, Dover, Mineola, N. Y., 1983.
- Schmidt, R. A., Vertical profiles of wind speed, snow concentration and humidity in blowing snow, *Boundary Layer Meteorol.*, 23, 233–246, 1982.
- World Meteorological Organization, Revised instruction manual on radiation instruments and scientific measurements, *WMO/TD 149*, edited by C. Frohlich and J. London, 140 pp., World Clim. Res. Prog., World Meteorol. Org.–Int. Council of Sci. Unions, Geneva, 1986.

D. W. Cline, National Operational Hydrologic Remote Sensing Center, Office of Hydrology, National Weather Service, 1735 Lake Drive West, Chanhassen, MN 55317-8582. (e-mail: cline@nohsrc.nws.gov)

(Received June 28, 1996; revised November 12, 1996; accepted December 31, 1996.)